Quantitative determination of atomic buckling of silicene by atomic force microscopy

Rémy Pawlak[a,1], Carl Drechsel[a], Philipp D'Astolfo[a], Marcin Kisiel[a], Ernst Meyer[a], and Jorge Iribas Cerda[b,1]

[a]Department of Physics, University of Basel, CH 4056 Basel, Switzerland; and [b]Instituto de Ciencia de Materiales de Madrid (ICMM), Consejo Superior de Investigaciones Cientificas (CSIC), 28049 Madrid, Spain

Edited by Robert J. Cava, Department of Chemistry, Princeton University, Princeton, NJ, and approved November 21, 2019 (received for review August 5, 2019)

The atomic buckling in 2D "Xenes" (such as silicene) fosters a plethora of exotic electronic properties such as a quantum spin Hall effect and could be engineered by external strain. Quantifying the buckling magnitude with subangstrom precision is, however, challenging, since epitaxially grown 2D layers exhibit complex restructurings coexisting on the surface. Here, we characterize using low-temperature (5 K) atomic force microscopy (AFM) with CO-terminated tips assisted by density functional theory (DFT) the structure and local symmetry of each prototypical silicene phase on Ag(111) as well as extended defects. Using force spectroscopy, we directly quantify the atomic buckling of these phases within 0.1-Å precision, obtaining corrugations in the 0.8- to 1.1-Å range. The derived band structures further confirm the absence of Dirac cones in any of the silicene phases due to the strong Ag-Si hybridization. Our method paves the way for future atomic-scale analysis of the interplay between structural and electronic properties in other emerging 2D Xenes.

silicene | buckling | defects | atomic force microscopy | density functional theory

Since the mechanical exfoliation of a single graphene layer from graphite (1), analogous monospecies 2D materials, generically termed Xenes, have attracted much interest in recent years, leading to the synthesis of silicene (2), germanene (3), stanene (4), and many others (5). In contrast to the flat sp^2 nature of the graphene hexagonal network, most Xenes exhibit a prominent buckling at the atomic scale due to their larger bond lengths which impede an efficient π-π overlap, thus promoting a mixture of sp^2/sp^3 bondings. Rather than a drawback, this lack of flatness is recognized as an opportunity to achieve exciting quantum phases, particularly the quantum spin Hall (QSH) (6), as massless Dirac fermions need not be destroyed while the spin–orbit coupling may be significantly enhanced by the corrugation (5). To date, however, quantifying atomic buckling of Xenes using diffraction techniques can be limited by their complex restructuring or the presence of defects while height estimation by means of scanning tunneling microscopy (STM) is often hampered by the convolution of topographic and electronic features.

The recent advent of high-resolution AFM imaging operated at low temperature with functionalized CO tips (7) has opened new avenues into the real-space imaging with improved lateral resolution of aromatic molecules (8) and 2D materials (9–13). Moreover, force spectroscopy enables one to quantitatively measure tip–sample forces (14) allowing, for instance, height determinations at surfaces (15–18) as well as the chemical identification of single atomic species (19, 20). In this context, AFM imaging and force spectroscopy combined with numerical calculations offer new opportunities to disentangle structural and electronic properties of epitaxial Xenes at the atomic level, specifically their intrinsic atomic buckling with subangstrom resolution.

Silicene stands as the paradigm of buckled Xenes. Many silicene-related exotic properties have been predicted or realized, such as superconductivity (21), giant magnetoresistance (22), tunable topological phases (23), long-ranged 2D ferromagnetic ordering (24), or even a transistor (25). Since the seminal work of Vogt et al. (2) where it was characterized on an Ag(111) surface, silicene has been grown only on a few other substrates, namely Ir(111) (26), ZrB_2(0001) (27), MoS_2(0001) (28), and Ru(0001) (29). On Ag(111), its properties have been scrutinized via a plethora of techniques including STM (2, 30–34), atomic force microscopy (AFM) (35–38), or angle-resolved photoemission spectroscopy (ARPES) (2, 39–41) among many others (42–44) as well as by extensive density functional theory (DFT) calculations (2, 32, 34, 45–47). Three highly reproducible atomically thin silicene phases have been reported with corresponding Si/Ag commensurate lattices: $(3\times3)/(4\times4)$, $(\sqrt{7}\times\sqrt{7})/(2\sqrt{3}\times2\sqrt{3})R30°$, and $(\sqrt{7}\times\sqrt{7})/(\sqrt{13}\times\sqrt{13})R13.9°$, denoted in the following 4×4, $2\sqrt{3}$, and $\sqrt{13}$, respectively. The former is the most studied one (2, 32–34, 43) and a general consensus now exists on its atomic and electronic structure. It corresponds to a 0.8-Å buckled honeycomb silicene sheet which, contrary to early claims, does not hold any Dirac-like cones around K/K′ due to a strong Ag/Si hybridization (39, 40, 42, 46, 47). Nevertheless, a recent ARPES study pointed to the presence of such cones around less symmetric k regions (40). The $2\sqrt{3}$ phase competes in stability with the 4×4 one as they often coexist but lacks long-ranged order. Local STM imaging for this

Significance

Most 2D materials possess a prominent atomic buckling, in contrast to their flat graphene counterpart. Upon epitaxial growth, complex restructuring, defects, and grain boundaries coexist on the surface with variable corrugations complicating an accurate determination using conventional diffraction techniques. To address this, we use atomic force microscopy with CO-terminated tips and numerical calculations to unveil the structure, local symmetry, and defects of a prototypical buckled 2D system, e.g., silicene on Ag(111). Based on site-dependent force spectroscopy, we provide a quantitative determination of the buckling magnitude of these phases with subangstrom precision. This method offers opportunities to study the interplay between structural and electronic properties in other emerging buckled systems with unprecedented resolution.

Author contributions: R.P. and E.M. designed research; R.P., C.D., P.D., and J.I.C. performed research; R.P., M.K., and J.I.C. analyzed data; and R.P. and J.I.C. wrote the paper.

The authors declare no competing interest.

This article is a PNAS Direct Submission.

Data deposition: The raw data reported in this paper have been deposited in Zenodo, https://zenodo.org/record/3501355.

[1]To whom correspondence may be addressed. Email: remy.pawlak@unibas.ch or jcerda@icmm.csic.es.

This article contains supporting information online at https://www.pnas.org/lookup/suppl/doi:10.1073/pnas.1913489117/-/DCSupplemental.

First published December 23, 2019.

phase typically reveals a broken moiré pattern formed by small $2\sqrt{3}$ moieties linked by low-lying Si atoms (30, 33). Again, a honeycomb lattice is the prevalent model with a DFT-derived buckling of 1.0 Å (45), although this value has not yet been experimentally corroborated by any diffraction technique. Last, the higher-temperature $\sqrt{13}$ phase has been paid less attention probably due to its complex restructuring and the limited resolution often found for this phase by STM and AFM experiments (38, 48). The generally accepted model contains 1, 2, and 3 upward-buckled Si atoms with a theoretical estimation of the corrugation of 0.9 Å (49).

For larger Si deposition rate and growth temperatures greater than 600 K, a $(\sqrt{3}\times\sqrt{3})R30°$ structure ($\sqrt{3}$) also emerged as crystallites on Ag(111). First interpreted as "multilayer silicene" (50), subsequent works suggest that it results from the formation of a Si-Ag surface alloy (51–54). Such significant interplay between Si atoms and the Ag substrate has also been observed in silicene nanoribbons on Ag(110) (55, 56).

Here we employ local STM and AFM imaging at low temperature (5 K) with CO-functionalized tips to characterize atomically thin silicene phases on Ag(111). Using force spectroscopy, we provide an accurate and local determination of the intrinsic buckling of each phase, a parameter of paramount importance to foresee the details in their electronic structures. High-resolution AFM and STM images allow an unambiguous identification of the local symmetry and chirality nature of the 4×4, $2\sqrt{3}$, and $\sqrt{13}$, respectively. Whereas local imaging supported by theoretical simulations confirms the 4×4 and $2\sqrt{3}$ structures, they clearly rule out the model in refs. 32 and 33 for the $\sqrt{13}$ phase, but confirm instead 1 of the 2 models proposed in ref. 45. Additionally, the systematic structural analysis by AFM sheds additional light on the defects present within the silicene adlayers (typically at the boundaries between domains) such as line defects or glassy-like regions comprising distorted pentagonal, hexagonal, or heptagonal Si rings. Force spectroscopy experimentally quantifies the atomic buckling of each silicene structure within 0.1 Å. The agreement between the structural details experimentally observed and those simulated from DFT optimizations permits a reliable analysis of their electronic structures. It turns out that the silicene/Ag hybridized surface bands/resonances are far more complex than what has been inferred so far from ARPES experiments, while no sign of Diracness is found in any of the 3 phases on Ag(111) (39–42, 46, 47, 49).

Results

Following preparations described in *Materials and Methods* and elsewhere (2, 32–34), the 4×4, $2\sqrt{3}$, and $\sqrt{13}$ silicene phases on

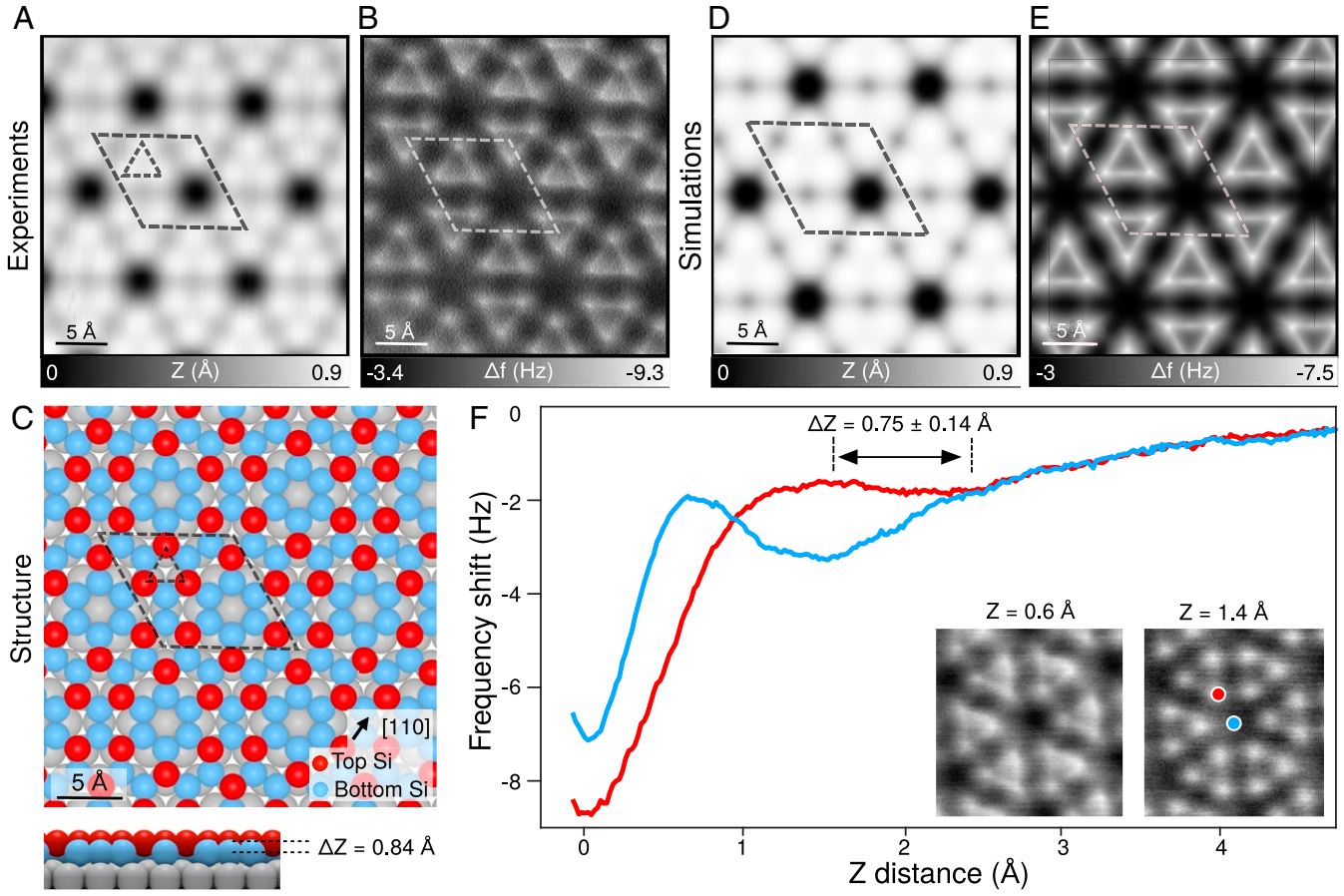

Fig. 1. The 4×4 silicene phase on Ag(111). (*A* and *B*) Experimental STM topography (*A*) and constant-height AFM image acquired with CO-terminated tips (*B*) at 4.5 K (STM, I = 1 pA, V = 0.2 mV; AFM, A = 0.5 Å, V = 0 mV). (*C*) Top and side representations of the 4×4 silicene structure optimized by DFT. The red and blue atoms are upmost and downmost silicon atoms of the silicene phase, respectively. (*D* and *E*) Simulated STM topography (*D*) and AFM images (*E*) from the relaxed structure. (*F*) Site-dependent force spectroscopic measurement, $\Delta f(Z)$, above the 4×4 upmost (red) and downmost (blue) atoms, each presenting a local minimum. The vertical dashed lines show the Z positions of upmost/downmost Si atoms analytically determined from force spectroscopy (*Materials and Methods*), allowing an estimate of the buckling magnitude ΔZ. *Insets* are constant-height AFM images acquired at $Z = 0.6$ Å and $Z = 1.4$ Å, respectively. The location of each curve corresponds to the colored circles in *Right Inset*.

Ag(111) were synthesized in ultrahigh vacuum, always obtaining extended domains over several tens of nanometers. Typical STM topographies of these phases are provided in *SI Appendix*, Figs. S1 and S2. Note that the $\sqrt{3}$ phase was not studied, since it consists of a sp^3-hybridized phase terminated with Ag atoms (51–54).

Our analysis of the atomic buckling of these structures is based on force spectroscopy allowing, in principle, apparent height determination with errors of the order of just a few picometers (10, 12, 15). To quantify bucklings with subangstrom precision, we used throughout this work an elaborated method consisting of 1) extracting force–distance $F(Z)$ curves from each of the van der Waals corrected $\Delta f(Z)$ spectra acquired above the upmost/downmost Si atoms of the silicene structure and 2) fitting the $F(Z)$ curves using an appropriate potential (*Materials and Methods*) to accurately determine the height position Z_0 of the atoms attributed to a local minimum/inflection point in the $\Delta f(Z)/F(Z)$ spectra. The height difference between these atom positions, $\Delta Z = Z_0^{\mathrm{top}} - Z_0^{\mathrm{down}}$, then corresponds to the buckling magnitude. Further details can be also obtained in *Materials and Methods* and *SI Appendix*, Fig. S4.

The 4 × 4 Silicene Phase. Although this phase is considered to be well characterized, we study it here for the sake of completeness as well as to assess the validity of our experimental approach to accurately determine the silicene buckling. Fig. 1 *A* and *B* shows an STM topographic and the corresponding constant-height AFM images, respectively, acquired for the 4×4 phase with a CO-terminated tip at 5 K. Both images show the well-known hexagonal arrangement of triangle-like patterns (marked with dashed lines) with an overall $p3m$ symmetry. The side of these triangles is $\sim$3.75 $\pm$ 0.05 Å. The theoretically optimized structure is displayed in Fig. 1*C*. In close agreement with previous results (2, 32–34, 43), it presents protruding Si atoms (red atoms) forming triangles with a side length of 3.86 Å while the corrugation between the upmost and downmost Si atoms is 0.84 Å. The associated STM/AFM simulations including the CO tip termination are shown in Fig. 1 *D* and *E*. Both indicate a good agreement with their experimental counterparts, allowing us to identify the triangular contrast in the AFM images caused by the 3 upmost Si atoms in each buckled hexagonal ring.

To experimentally quantify the atomic buckling, we acquired site-dependent frequency shift curves as a function of tip–sample separation $\Delta f(Z)$ above the upmost (red) and downmost (blue) Si atoms of the structure (Fig. 1*F* and *SI Appendix*, Fig. S4*A*). At large tip–sample separations ($Z \geq 2.5$ Å), only long-range electrostatic contributions are probed since the tails of the

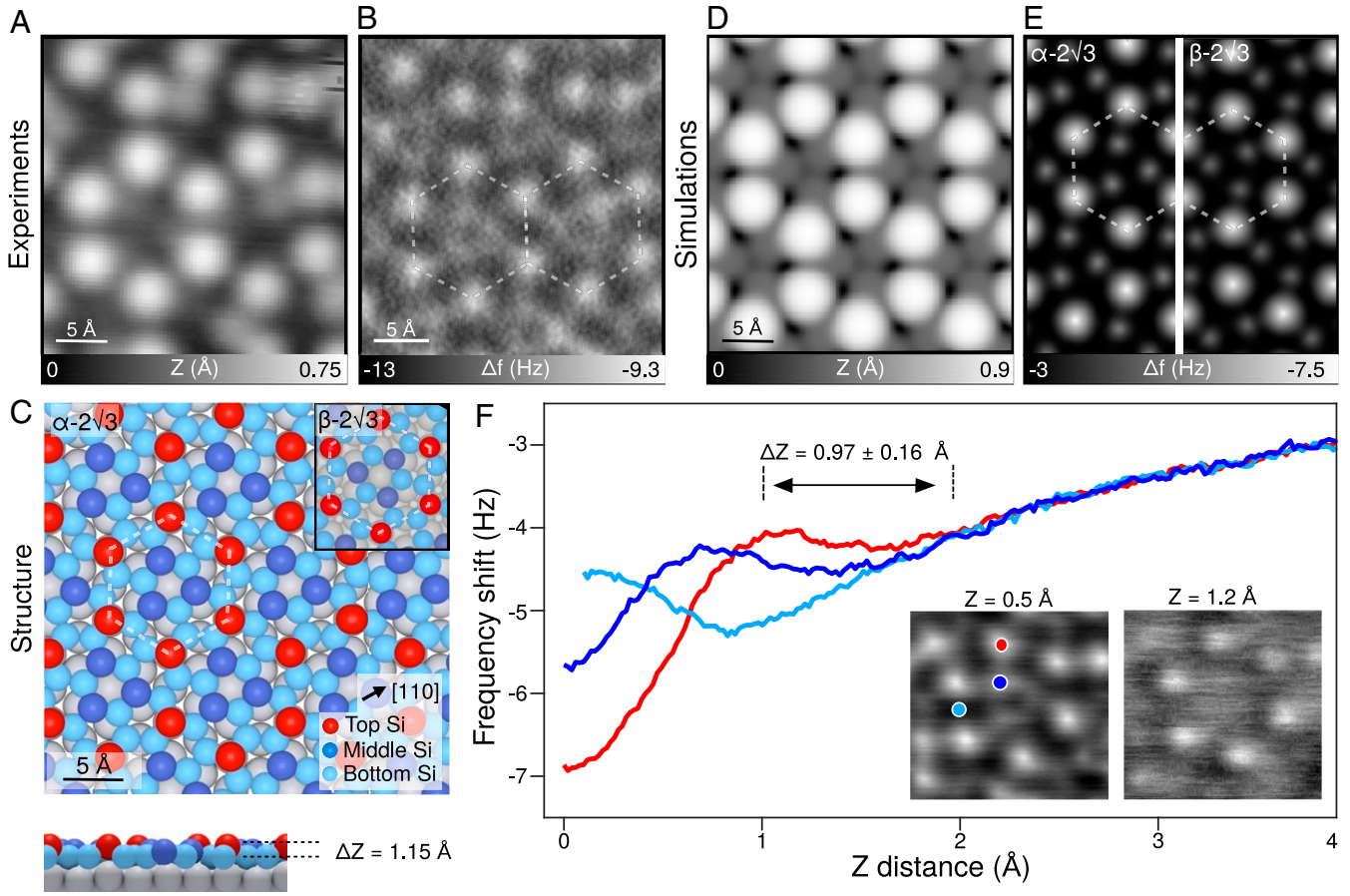

Fig. 2. The $(2\sqrt{3} \times 2\sqrt{3})R30^\circ$ silicene phase on Ag(111). (*A* and *B*) Experimental STM topography (*A*) and constant-height AFM image (*B*) acquired with CO-terminated tips at 4.5 K (STM, I = 1 pA, V = 0.2 mV; AFM, A = 0.5 Å, V = 0 mV). (*C*) Top and side representations of the relaxed structure $\alpha - (2\sqrt{3} \times 2\sqrt{3})R30^\circ$ on Ag(111). The white hexagons correspond to the ones shown in *B*. *Inset* shows the $\beta - 2\sqrt{3}$ structure, the chiral counterpart of $\alpha - 2\sqrt{3}$. (*D*) Simulated STM topography for the $\alpha - 2\sqrt{3}$ atomic structure. (*E*) Simulated AFM images of the $\alpha-$ and $\beta - 2\sqrt{3}$ structures. (*F*) Site-dependent $\Delta f(Z)$ curves acquired above the upmost (red), downmost (pale blue), and intermediate (dark blue) Si atom positions, respectively. The vertical dashed lines indicate the Z positions of the red and pale blue atoms analytically determined by force spectroscopy (*Materials and Methods*), allowing an estimate of the buckling magnitude ΔZ. *Insets* are constant-height AFM images acquired at tip–sample separations of $Z = 0.5$ Å and $Z = 1.2$ Å, respectively. The colored circles correspond to the location where each curve was acquired.

spectra merge into the same line. At closer tip–sample distances (below $Z = 2.5$ Å), each $\Delta f(Z)$ curve shows a "local minimum" followed by a "bump" arising from site-specific interactions between the front end oxygen atom of the CO-terminated tip apex and the probed Si atom. In Fig. 1*F*, the dashed vertical lines indicate the bottom of the dips analytically determined for the red and blue atoms, respectively (details in *Materials and Methods*). Their Z positions in principle give a good estimate of their relative heights with respect to the tip–sample distance, which are also well reflected in the corresponding constant-height AFM images (Fig. 1 *F*, *Insets*). For the upmost Si atoms (red curve), the minimum is located at $Z = 2.42 \pm 0.08$ Å whereas for the lower Si atoms (blue curve) it is at $Z = 1.67 \pm 0.05$ Å. We interpret this difference, ΔZ, as a direct determination of the buckling in the 4×4 silicene phase. The obtained intrinsic buckling $\Delta Z = 0.75$ Å is in excellent agreement with previous results (2, 32, 57).

The $(2\sqrt{3} \times 2\sqrt{3})R30°$ Silicene Phase ($2\sqrt{3}$). With the same strategy, we next characterize the $2\sqrt{3}$ silicene phase (Fig. 2). In STM overviews (*SI Appendix*, Fig. S1 *B* and *C*), this phase always appears as a disrupted moiré pattern consisting of moieties with a $(2\sqrt{3} \times 2\sqrt{3})R30°$ hexagonal arrangement surrounded by interconnected defected narrow regions. We assign the absence of a long-ranged moiré pattern, as typically encountered for graphene on metals, to the weaker Si-Si bonds in silicene which cannot hold the tensile strain induced. Indeed, and since the $2\sqrt{3}$ phase is compressed, it has been argued that the disordered regions correspond to expanded defected areas of the silicene honeycomb lattice (58).

Fig. 2*A* shows a close-up STM image of 2 adjacent hexagons within a $2\sqrt{3}$ ordered patch. Each of them is made up of 6 protrusions, with a distance between them of 5.2 Å, about 2 times larger than the expected Si-Si interatomic distance in silicene (2.4 Å). The corresponding constant-height AFM image (Fig. 2*B*) resolves equally well such a hexagonal arrangement (white dashed lines), but additionally reveals a triangular pattern inside the hexagon with a side length (~0.36 Å) comparable to that of the triangles in the (4×4) phase.

The rotation angle between the silicene and Ag(111) lattices reduces the symmetry of the combined system to $p3$, thus allowing for the coexistence of 3 degenerate mirror symmetric domains. For each domain, there are 3 symmetry-preserving possible stackings between the silicene and the Ag substrate plus another 3 obtained after inverting the silicene layer. Among them, our DFT-derived energetics corroborate the model of refs. 33 and 45 shown in Fig. 2*C*, where atoms colored in light blue, dark blue, and red correspond to the downmost, intermediate, and upmost Si atoms, respectively. The structure, denoted as the

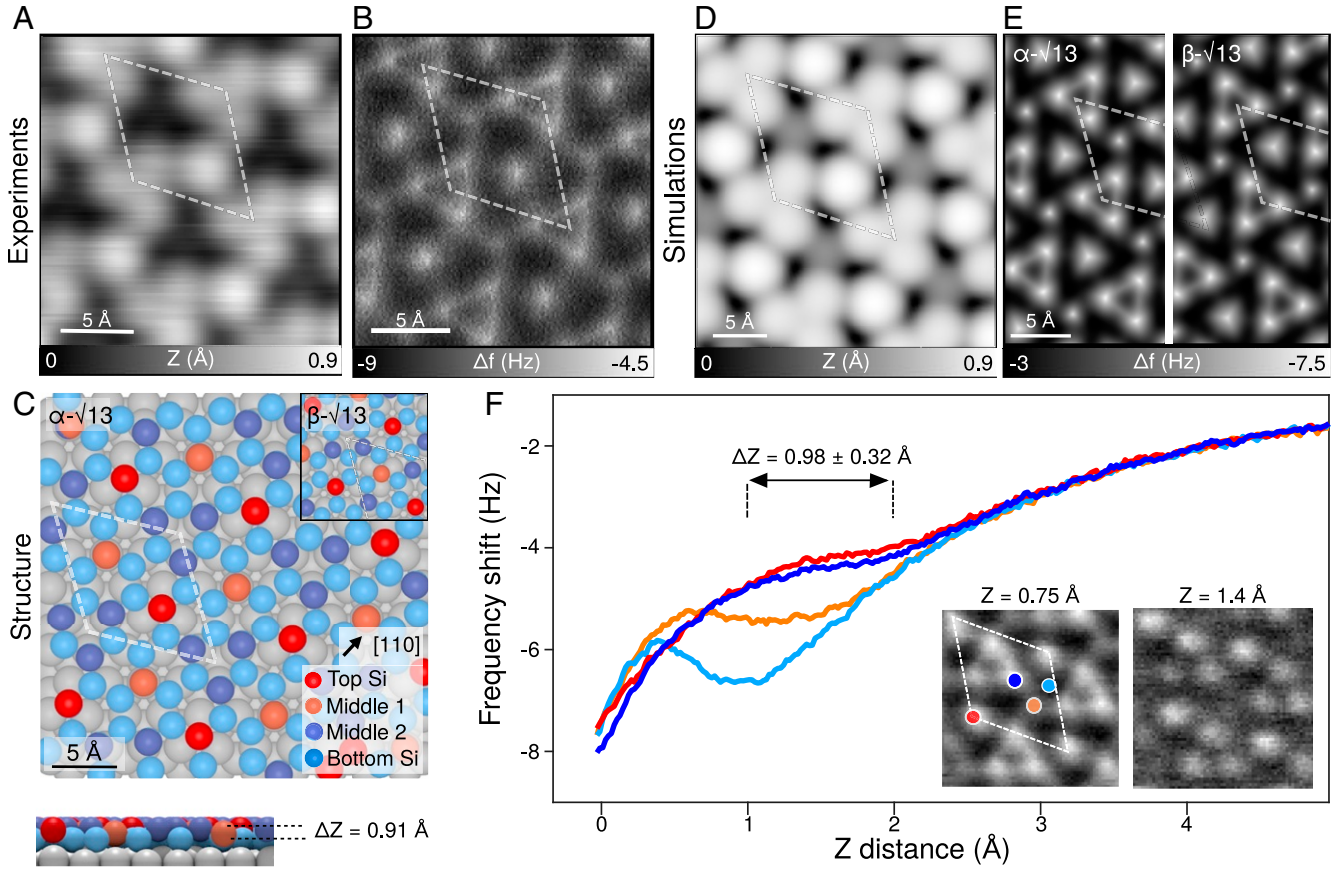

Fig. 3. The $(\sqrt{13} \times \sqrt{13})R13.9°$ silicene phase on Ag(111). (*A* and *B*) Experimental STM topography (*A*) and constant-height AFM image (*B*) acquired with CO-terminated tips at 4.5 K (STM, I = 1 pA, V = 0.2 mV; AFM, $A = 0.5$ Å, $V = 0$ mV). (*C*) Top and side representations of the relaxed $\alpha - \sqrt{13}$ phase. The white frameworks correspond to the observed unit cells in STM images. *Inset* shows the $\beta - \sqrt{13}$ structure. (*D*) Simulated STM topography of the $\alpha - \sqrt{13}$ atomic structure relaxed by DFT. (*E*) Simulated AFM image of the $\alpha - \sqrt{13}$ and $\beta - \sqrt{13}$ structures. (*F*) Site-dependent $\Delta f(Z)$ spectra acquired above the upmost (red), first intermediate (purple blue), second intermediate (orange), and downmost (pale blue) atoms, respectively. The vertical dashed lines indicate the Z positions of upmost/downmost Si atoms analytically determined from force spectroscopy (*Materials and Methods*), allowing an estimate of the buckling magnitude ΔZ. *Insets* show AFM images acquired above the $\beta - \sqrt{13}$ structure at $Z = 0.75$ Å and $Z = 1.4$ Å. The colored circles correspond to the locations where the force curves were acquired.

$\alpha - 2\sqrt{3}$ phase, consists of one low-buckled hexagon (0.55 Å) centered at a top site, surrounded by 6 high-buckled hexagons (1.15 Å) due to a Si atom residing at a top site. The simulated STM and AFM images for this model (Fig. 2 *D* and *E*) reproduce the experimental data, with the brightest protrusions arising from the top Si atoms (red) and the inner triangle from the 3 higher-lying ones (dark blue) in the low-buckled hexagon.

Remarkably, the AFM image in Fig. 2*B* reveals the coexistence of 2 mirror chiral structures side by side, as the inner triangles point in opposite directions between the marked hexagon and that to its right. Since the mirror plane relating both triangles is not aligned with any of the Ag(111) mirror planes, both structures have necessarily an inequivalent symmetry. The inversion of the inner triangle may be then explained by a 180° rotation of the silicene layer resulting in the $\beta - 2\sqrt{3}$ phase shown in the inset of Fig. 2 *C*, Inset. Since the 2 phases differ only in the registry of the subsurface silver layer, they are almost degenerate (quasi-enantiomers), with a marginal DFT-derived energy difference of 6 meV. Indeed, by combining their simulated AFM images (Fig. 2*E*), a good match with the experimental image of Fig. 2*B* is achieved.

The atomic buckling of the $2\sqrt{3}$ structure was again determined from the precise analysis of site-dependent force spectroscopic measurements (*Materials and Methods* and *SI Appendix*, Fig. S4*B*). Fig. 2*F* shows 3 $\Delta f(Z)$ curves acquired above the upmost (red), intermediate (dark blue), and downmost (pale blue) Si sites according to Fig. 2C. Similar to the 4×4, the fingerprint of the atom heights is the Z position of the local minimum in each $\Delta f(Z)$ curve (marked by vertical dashed lines), whose precise value is derived from the fitting protocol described in *Materials and Methods*. The resulting buckling between the upmost and intermediate atoms is $\Delta Z = 0.71 \pm 0.16$ Å, while the overall corrugation (difference between upmost and downmost Si atoms) is $\sim 0.97 \pm 0.22$ Å. The former is in good agreement with the DFT-derived value, whereas the second value is about 0.1 Å smaller than the theoretical one, although we note a larger uncertainty in the precise location of the red minimum (hence the increased error bar for the overall buckling).

The ($\sqrt{13} \times \sqrt{13}$)*R*13.9° Silicene Phase ($\sqrt{13}$). Large-scale images of the $\sqrt{13}$ phase (Fig. 3 *A* and *B* and *SI Appendix*, Fig. S1 *D–F*) reveal the coexistence of 2 apparently mirror-symmetric domains separated by multiple defected lines (domain walls) forming 120° among them. Vortex-like features are readily seen arising from the intersection of 6 of such defected segments. Remarkably, the vortices are regularly arranged, leading to a large, somewhat imperfect moiré-type hexagonal superstructure with a distance of ~5.0 nm between vortices. The images agree well with those of Liu et al. (59), who reported an approximate $(5\sqrt{3} \times 5\sqrt{3})$R12° moiré pattern.

Fig. 3 *A* and *B* shows high-resolution STM and AFM images of one of the domains. The $\sqrt{13}$ supercell (white rhombus in both images) is characterized by a triangle with edges 3.6 Å long, which in analogy to the previous phases, is associated to a buckled Si hexagonal ring. At the epicenter of the lower half-unit cell (HUC) both maps present a brighter protrusion, while a second less intense bump at the upper HUC and faintly connected to the vertexes of the 3 surrounding triangles is resolved only in the AFM image. Despite the complexity of the pattern, it displays a clear $p3$ symmetry, with 3 possible rotation axes: in the triangle's epicenter as well as in either of the 2 bumps.

In the DFT optimization we considered 2 different relative rotation angles for the pseudo-(1×1) silicene lattice and, for each of them, 3 possible symmetry-preserving stackings between the silicene and the Ag(111) substrate plus the analogous structures after inverting the silicene layer. The most stable structure, denoted as $\alpha - \sqrt{13}$, is shown in Fig. 3*C*: It contains a protruding Si atom (colored in red); a low-buckled hexagon (dark and pale blue), this time centered at an *hcp* site; and an extra 3-fold coordinated silicon at an *fcc* site (orange). A relative agreement is again found between the AFM simulations for this model ($\alpha - \sqrt{13}$ in Fig. 3*E*) and the experimental counterpart, allowing a straightforward identification of all subtle features; in particular, the dimmer bump in the AFM image corresponds to the orange Si atom in Fig. 3*C*.

On the other hand, and following similar symmetry arguments to those discussed for the previous $2\sqrt{3}$ phase, the second $\sqrt{13}$ domain displaying inverted triangles may be associated to an inversion of the silicene adlayer, leading to the symmetry-inequivalent $\beta - \sqrt{13}$ phase shown in Fig. 3 *C*, *Inset*. Again, its main difference with respect to the α domain is the registry of the second silver layer, so that the orange atom now resides at an *hcp* site and the buckled hexagon is inverted and centered at an *fcc* site (Fig. 3 *C*, *Inset*). The associated AFM simulation, shown in Fig. 3*E*, is practically identical to that of the α phase after performing a 180° rotation, in agreement with experiment. Energetically, the stability of the 2 structures is very close (within 10 meV). In fact, the β model was already proposed as a plausible candidate for the $\sqrt{13}$ phase, yielding a very similar STM image to that in Fig. 3 *A* and *D* (45, 60).

Fig. 3*F* displays the $\Delta f(Z)$ spectra acquired above the relevant atomic sites (shown in Fig. 3 *F*, *Left Inset* by colored circles). Each curve exhibits a local minimum (strictly speaking, an inflection point for the red and dark blue curves), whose Z position directly correlates with the relative height of the corresponding Si atoms (*SI Appendix*, Fig. S4*C*). The maximal experimental buckling ($\Delta Z = 0.98 \pm 0.32$ Å), corresponding to the height difference between the red (upmost atoms) and pale blue (downmost) curves, is in good agreement with the DFT value (0.91 Å), while the height difference between the upmost red and dark blue atoms (0.1 Å) is identical to the theoretical value.

Comparison between Atomic Buckling Determined via Force Spectroscopy and State of the Art. To date, the intrinsic atomic buckling of silicene structures was obtained by combining STM imaging or X-ray diffraction techniques at room temperature with DFT calculations (57, 61). Although STM possesses a picometer precision in the Z direction, the technique is primarily sensitive to LDOS that can hamper an accurate buckling estimation. With a similar Z precision, X-ray techniques can also lack sensitivity due to the large number of atomic configurations in the silicene structures and the coexistence of several phases on the surface as well as the presence of disordered Si domains (*SI Appendix*, Fig. S2). In contrast, force spectroscopy probes local force interactions arising between the last front atom of the tip and the sample, allowing apparent height determination with errors of the order of just a few picometers (10, 12, 15).

Table 1 summarizes the estimated buckling, $\Delta Z = Z_0^{\max} - Z_0^{\min}$, and the associated fit errors of the 4×4, $2\sqrt{3}$, and $\sqrt{13}$ phases as well as those obtained from DFT. $d_{Si/Ag}$ refers to

Table 1. Summary of intrinsic buckling of the 4×4, $2\sqrt{3}$, and $\sqrt{13}$ phases obtained from DFT, ΔZ_{DFT}, and force spectroscopy, ΔZ_{exp}

	ΔZ_{DFT}, Å	ΔZ_{exp}, Å	Refs. 45 and 60–62, Å
4×4	0.84	0.75 ± 0.14	0.84
$2\sqrt{3}$	1.15	0.97 ± 0.16	1.0–1.12
$\sqrt{13}$	0.91	0.98 ± 0.32	0.71–1.39
$d_{Si/Ag}$	2.4	1.8	2.4

$d_{Si/Ag}$ is the silicene height with respect to the Ag surface.

the relative height of the Si atom compared to the Ag surface. The experimental ΔZ values agree well with the theoretical ones for each phase, varying in the range of 0.75 to 0.97 Å (ΔZ_{exp}) and 0.84 to 1.15 Å (ΔZ_{DFT}), respectively. Our estimation of the buckling in the 4×4 and $2\sqrt{3}$ phases is also in agreement with previous theoretical works (~0.84 Å and ~1.12 Å) (60–62) whereas, for the $\sqrt{13}$ phase, larger discrepancies are obtained compared to values in the literature (0.71 to 1.39 Å) (49, 60, 61). Note finally that our buckling estimate extracted from low-temperature data agrees with most of the structures previously analyzed at room temperature. This suggests the absence of any substantial phase transition or lattice expansion/compression upon cooling.

Structure of the Line Defects in the $\sqrt{13}$ Phase. Fig. 4 *A* and *B* shows an STM overview and the corresponding AFM image of the $\sqrt{13}$ phase acquired around a vortex formed by the convergence of 6 defected lines (indicated by white dashed lines in Fig. 4*B*). These linear boundaries separate 2 domains with the triangular features at each side pointing in opposite directions (48). As mentioned above, both domains are not mirror symmetric but related by an inversion of the silicene layer ($\alpha-$ and $\beta-\sqrt{13}$ structures in Fig. 3*E*). A zoom-in of one of the line defects is presented in Fig. 4*D*, displaying a typical square pattern containing 4 maxima linked by pairs along the transversal direction. The distance between the paired protrusions is ~3.8 Å, slightly longer than the triangle edges associated to a buckled Si hexagonal ring, whereas the distance between pairs is ~4.0 Å. The STM image of the line defects (Fig. 4*A*) shows that the 4 protrusions forming the squares are by no means chemically equivalent, since the 2 Si atoms forming the diagonal normal to the line defect are clearly brighter than those at the other diagonal. According to force spectroscopic measurements (Fig. 4*F* and *SI Appendix*, Fig. S4*D*), the atomic buckling between the line defect atoms (gray and black curves) is identical (0.11 Å) to the intermediate Si atoms of the $\sqrt{13}$ phase (dark blue).

From the structural side, the line defects appear to involve a large restructuring at the boundaries between the 2 domains, although an elaborate model developed by Jamgotchian et al. (48) indicates that the silicene film remains a continuous honeycomb layer with only small deformations due to a compressive strain. Note that, in contrast with the $2\sqrt{3}$ phase, the $\sqrt{13}$ is expanded (48), so that the line defects and vortices tend to relieve the stress stabilizing this phase over large areas. To address the nature of the squared pattern experimentally observed and based on the knowledge of the precise domain geometries and the relative positions of the maxima in the images at each side of the boundary, a realistic atomistic model for the defected line can be derived. Our interface model consists of a 4-silver-layers slab using a (1×7) supercell with respect to the $\sqrt{13}$ cell comprising 3 unit cells of each domain (462 atoms in total) and considering a few different arrangements of the

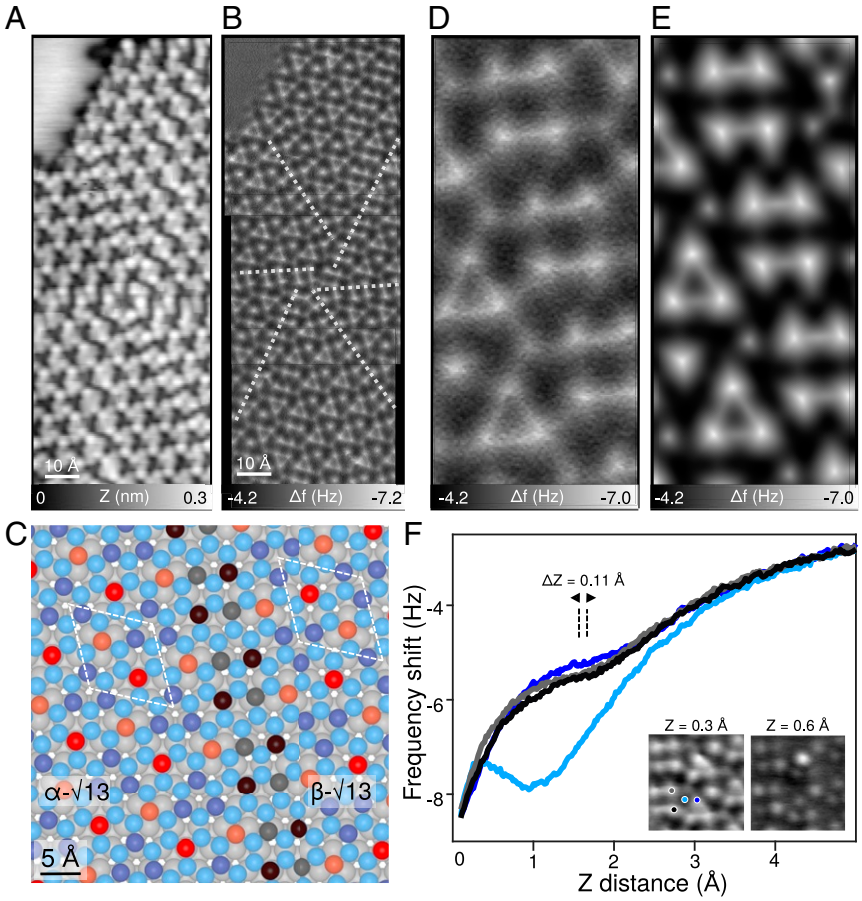

Fig. 4. Line structure of the $\sqrt{13}$ phase. (*A* and *B*) Overview STM (*A*) and AFM (*B*) images of the $\sqrt{13}$ moiré superstructure composed of line defects (white dashed lines) emerging from a vortex-like center. (*C*) DFT structure of the line structure between $\alpha-\sqrt{13}$ and $\beta-\sqrt{13}$ domains. (*D*) Zoom-in AFM image of the line defect. (*E*) Simulated AFM image obtained from the relaxed DFT structure. (*F*) $\Delta f(Z)$ spectra acquired above the square-like features (*Insets*). The vertical dashed lines show the *Z* positions of line defect Si atoms analytically determined from force spectroscopy (*Materials and Methods*), allowing an estimate of height difference between them. (Scan parameters: $A=0.5$ Å, $V=0$ V.)

PHYSICS

interfacial Si atoms. Fig. 4*C* presents the DFT relaxed structure that best matches the experimental AFM image, as judged from its simulated image displayed in Fig. 4*E* which, indeed, nicely reproduces the squared pattern as well as the bright lines connecting the bumps at each side of the squares. Notably, the silicene hexagonal network is not truncated at the boundary but remains fairly continuous, thus confirming the structural model of ref. 48. Within each square, 2 Si atoms reside at top sites (dark-colored balls in Fig. 4*C*) in equivalent positions to those they occupy in each $\sqrt{13}$ domain. The other 2 gray atoms are located close to a nearest-neighbor Ag site and, due to the stress induced at the interface, lie at the same height as the former ones. The difference in height between the 2 interface sites is 0.08 Å, again in close agreement with the 0.11-Å experimental value.

Dark STM Regions Are Disordered Si Adlayers. Previous works have reported the presence in STM images of dark regions at the first stage of the silicene growth. Appearing embedded into the surface (51), these regions were interpreted as silicon atoms incorporated into the substrate due to the formation of a Si-Ag alloy (51–54). We obtained similar STM contrasts (*SI Appendix*, Figs. S2, S5, and S6) at step edges or surrounding the silicene phases and analyzed them using force spectroscopy with CO-terminated tips.

Fig. 5*A* shows a representative constant-height AFM image of a dark STM region (*SI Appendix*, Fig. S1*G*) between a 4×4 and a $2\sqrt{3}$ silicene domain. The fact that it shows AFM contrast indicates that the relative atomic heights in this region should be similar to those in the adjacent ordered domains. On the other hand, the absence of contrast in the upper left corner corresponds to the clean Ag(111) region which is about 2.0 Å lower as estimated by constant-height imaging and force spectroscopy (*SI Appendix*, Fig. S3). This value is in reasonable agreement with DFT calculations, which places the average silicene height 2.4 Å above the surface.

A closer look at the AFM image in the dark region (Fig. 5*B*) reveals the signature of multiple structural motifs forming a "glassy-like" silicene region where buckled hexagons, pentagons, and heptagons appear interconnected, in line with other Si structures where nonhexagonal motifs have been predicted (56, 63, 64). A better estimate of the height difference among the 3 regions is obtained using force spectroscopy, as shown in Fig. 5*C* and *SI Appendix*, Fig. S4*E*, where we plot $\Delta f(Z)$ spectra recorded above the most protruding Si atoms of the 4×4 (dark blue), $2\sqrt{3}$ (red), and glassy (pale blue) regions, respectively. The maximal ΔZ of ~0.52 Å is found between the 4×4 and the glassy region whereas this value decreases to ~0.35 Å at the boundary with the $2\sqrt{3}$ domains. Note that this difference of 0.2 ± 0.1 Å agrees with the difference in intrinsic buckling among both phases (1.1 Å versus 0.8 Å). Thus we conclude that the dark STM regions correspond to Si adlayers with no sign of Ag-Si alloying as previously claimed (51–54).

Electronic Properties of the Silicene Phases. *SI Appendix*, Fig. S10 presents a summary of the electronic structure of the silicene phases described above. Their computed band structures, in the form of projected density of states (PDOS) (E, k) maps, are shown for the 4×4, $2\sqrt{3}$, and $\sqrt{13}$ structures. In each map, the projections on the Si atoms (blue) and the first Ag layer (red) have been superimposed on top of those corresponding to the subsurface layers (gray), which are already close to the bulk projections. Despite the profusion of bands across the Brillouin zones (BZs) due to backfolding and apart from a few faint resonances crossing E_F, all phases show a clear gap in the π bands which is consistent with the low DOS around the Fermi level in

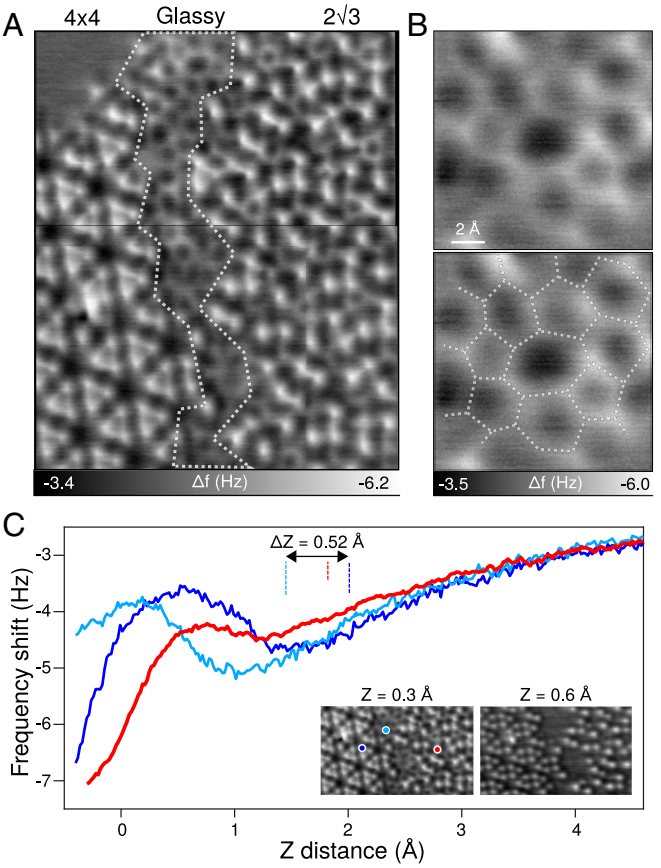

Fig. 5. Disordered silicene at boundaries. (*A*) Constant-height AFM image with a CO-terminated tip of a grain boundary between a 4×4 and a $2\sqrt{3}$ domain. The boundary region is delimited with white dashed lines. (*B*) Zoom-in AFM image of this region revealing buckled and highly distorted hexagonal, pentagonal, and heptagonal motifs (marked by white dashed lines in *Bottom* image). (*C*) $\Delta f(Z)$ spectra acquired above the upmost Si atoms of the 4×4 (dark blue), $2\sqrt{3}$ (red), and glassy (pale blue) regions, respectively. The vertical dashed lines show the Z positions of Si atoms of each phase analytically determined from force spectroscopy (*Materials and Methods*), allowing an estimate of height difference between them. *Insets* show AFM images acquired at $Z = 0.3$ Å and $Z = 0.6$ Å.

single-point dI/dV curves (*SI Appendix*, Fig. S5*C*) acquired for the $2\sqrt{3}$ and 4×4 cases.

Nevertheless, no sign of any Dirac cones localized within the silicene sheet appears in any of the phases. In agreement with previous observations (39, 40, 46, 47), all surface bands in the -2 to $+1$ eV region present a strong Si-Ag1 hybridization with parabolic dispersions characteristic of covalent bonding (in contrast with the linear metal bands). Further evidence for the absence of any pure sp^2 hybridization is provided by the following: 1) A decomposition of the Si PDOS in terms of its angular momentum contributions (*SI Appendix*, Fig. S7) reveals a strong p_z and p_{xy} mixing around E_F and 2) π^* bonding among the Si atoms appears only at around $+1$ eV (see the local DOS maps in *SI Appendix*, Fig. S8).

Notwithstanding, a complete and unambiguous characterization of the silicene surface bands on Ag(111) has not yet been accomplished, mainly due to the overwhelming bulk silver signal in ARPES experiments as well as to the many umklapp processes leading to additional metal bands in the spectra (41). The recent work of Feng et al. (40) on the 4×4 phase is probably the one probing the largest number of Si surface bands, especially along the $K - M - K'$ direction, where the existence of 2 p- doped Dirac cones was concluded, in contrast with the PDOS(k, E)

maps of *SI Appendix*, Fig. S10. To address this discrepancy, Fig. 6 shows a direct comparison between these ARPES data and the calculated Si-PDOS maps along the same k directions. In the latter maps we have superimposed the bulk Ag (unfolded) contribution in green. Along $\Gamma - K$ and $\Gamma - M$ there is a close relationship (within the expected DFT accuracy) between the highly dispersive bulk band edges and the photoemitted curves, which is consistent with a much larger silver ARPES signal that hides the Si-derived one. Along the $K - M - K'$ direction, on the other hand, large metal gaps exist, which allow an unambiguous identification of the surface state bands. Indeed, the calculated Si projections reproduce nicely the highly dispersive bands denoted by S, while the electron pocket at Γ (EP) could be ascribed to the intense bulk band edge minimum (~ -0.3 eV) or the minimum of another Si band (S′) or even both. In either case our DFT results rule out the existence of a pair of Dirac cones.

Discussion

We have provided an in-depth structural analysis of the various silicene structures on Ag(111), using low-temperature atomic force microscopy with CO-terminated tips assisted by density functional theory. From precise force spectroscopic measurements acquired on specific Si atoms of each silicene phase, we have quantified with subangstrom vertical precision their atomic bucklings in the 0.8- to 1.1-Å range, always in agreement with the corrugations obtained from the DFT relaxations. Local AFM imaging for the lower-symmetry $2\sqrt{3}$ and $\sqrt{13}$ phases reveals a quasichiral character, whereby 2 almost degenerate structures (α and β) coexist within each phase, either at a very local level ($2\sqrt{3}$ case) or forming well-ordered and separated domains ($\sqrt{13}$). The α and β structures are related by a 180° rotation of the silicene layer about the surface normal which inverts the registry of the Si atoms with respect to the subsurface Ag(111) plane (hcp sites transform into fcc sites and vice versa). Remarkably, a detailed study of the structure of the domain boundaries (multiple line defects) in the $\sqrt{13}$ phase shows that the silicene honeycomb arrangement is essentially preserved throughout the surface. From the elucidated silicene structures, we computed their band structure under a semiinfinite geometry. While the $2\sqrt{3}$ and $\sqrt{13}$ free-standing silicene phases possess a linear dispersion near the Fermi level that slightly differs due to their intrinsic atomic buckling (*SI Appendix*, Fig. S9), the interaction with the Ag(111) systematically leads to the disappearance of the Dirac cone and the emergence of strongly hybridized Ag-Si states as previously observed (39, 40, 46, 47).

We emphasize that our AFM/DFT-based approach is self-contained to determine precisely the structure of silicene and other monoelement Xenes with high lateral precision, but also their local atomic bucklings independent of their structural complexity. Our results also suggest the importance of controlling the atomic buckling in 2D silicene in future synthesis processes or exfoliation onto nonconductive substrates to preserve their electronic properties. We are thus convinced that such systematic investigation will help in foreseeing the precise structural characterization of analogous 2D materials where atomic buckling defects could lead to novel exotic properties (5).

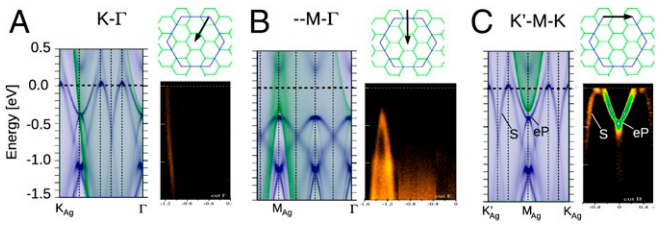

Fig. 6. Comparison between ARPES measurements of ref. 40 and PDOS(k, E) for the 4×4 phase. (*A*–*C*) Band structure along k paths $K_{Ag} - \Gamma$ (*A*), $M_{Ag} - \Gamma$ (*B*), and $K'_{Ag} - M_{Ag} - K_{Ag}$ (*C*), respectively, as indicated by the black arrows in *Insets* displaying the BZ scheme. In *A*–*C*, *Right* the map corresponds to ARPES data and in *A*–*C*, *Left* to the calculated Si PDOS (blue) with the bulk Ag contribution superimposed on top (green). Data from ref. 40.

Materials and Methods

Sample Preparation. The Ag(111) single crystal was purchased from Mateck GmbH and cleaned by several cycles of sputtering and annealing in ultrahigh vacuum (UHV). Silicon was evaporated from a Si wafer heated up to 1,300 K onto the silver surface. The Si flux was estimated using a quartz microbalance to ≈0.05 monolayer per minute. To obtain the silicene phases, we annealed the Ag(111) during deposition at the appropriate temperatures reported elsewhere (32, 34).

STM/AFM Imaging. The STM/AFM experiments were carried out at 4.8 K with an Omicron GmbH low-temperature STM/AFM operated with Nanonis RC5 electronics. We used commercial tuning-fork sensors with a chemically etched tungsten tip in the qPlus configuration (f_0 = 26 kHz, Q = 10,000 to 25,000, nominal spring constant k = 1,800 N·m^{-1}, oscillation amplitude $A \approx$ 50 pm). The tip apex was ex situ sharpened by milling with a focused ion beam. The constant-height AFM images were acquired with CO-terminated tips operated in the noncontact mode and at zero voltage. For that, CO was dosed onto the sample kept at low temperature. Prior to its functionalization, the apex was gently indented into the silver surface at low temperature, leading to a silver-coated apex. Then, a single CO molecule was vertically manipulated from the silver surface onto the tip following the procedure described in refs. 8 and 65, resulting in a CO-terminated tip with the carbon atom toward the metal tip (66, 67). Different tips were prepared that way throughout the study. All voltages refer to the sample bias with respect to the tip. Differential conductance single spectra and maps shown in SI Appendix were carried out with the lock-in technique (f = 540 Hz, V_{mod} = 10 mV).

Force Spectroscopy. Force spectroscopic measurements were obtained using CO-terminated tips. To provide an accurate estimate of the intrinsic buckling in silicene, we subtracted from each experimental $\Delta f(Z)$ dataset the van der Waals background (estimated from a single 5-nm-long $\Delta f(Z)$ spectrum) and then extracted the associated force–distance curves $F(Z)$ using the Sader–Jarvis algorithm (68) (*SI Appendix*, Fig. S4). $F(Z)$ spectra were then fitted with the derivative of the Coulomb–Buckingham pairwise potential (69), which is used to reproduce interatomic Si-O bonds in numerical simulations of silica. This potential, $V(Z)$, consists of a long-range Coulomb term and short-range contributions adopting the usual Buckingham form (70) and varies with the interatomic distance Z as

$$V(Z) = Ae^{-B(Z-Z_0)} - \frac{C}{(Z-Z_0)^6} + \frac{D}{4\pi\epsilon_0 Z},$$

where Z_0 represents the relative height of the protruding Si atom in silicene. The long-range Coulomb contribution is defined by a single fitting parameter D, with ϵ_0 is the vacuum permittivity. The parameters A, B, and C account for the short-range Buckingham force interactions. Note that our fits do not consider the force contributions arising from the tip which, in turn, produces small discrepancies at short Z distances. It is also worth mentioning that the Lennard-Jones potential conventionally used to fit force spectroscopic data failed to satisfactorily reproduce the shape of the $F(Z)$ spectra. The Z_0 positions of the local minima in each $\Delta f(Z)$ spectrum (marked by dashed lines in the figures) were analytically determined by fitting the position of the inflection point in the $F(Z)$ curves. The fit results and the associated errors are shown in *SI Appendix*, Fig. S4 and Table 1.

Theoretical Details. The GREEN package (71) and its interface to the SIESTA (72) pseudopotential DFT package under the generalized gradient approximation (73) (GGA) have been employed for the atomic relaxations as well as for the calculation of the electronic properties and the STM simulations. All atoms were described via strictly localized atomic orbitals following a double-ζ polarized (DZP) scheme (72) with confinement energies of just 20 meV for the Si and first Ag layer atoms and 100 meV for the rest of the bulk-like silver atoms. Other calculation parameters were set to the following values: a 0.06-Å resolution in the real-space mesh (700 Ryd cutoff), a k

sampling of $\sim(24 \times 24)$ relative to the Ag(111) 2D lattice, and an electronic temperature (Fermi–Dirac smearing) of $kT = 100$ meV.

The model systems for all trial 4×4, $2\sqrt{3}$, and $\sqrt{13}$ structures initially comprised 4 Ag layers thick slabs allowing all Si and the first 2 metal layers to relax until forces were smaller than 0.02 eV·Å^{-1} while the 2 bottom layers were fixed to bulk-like positions employing the GGA-optimized Ag lattice parameter (a = 4.15 Å) which is only 1.6% larger than the experimental one. The most stable structures for each phase were further reoptimized, including up to 8 substrate layers.

The surface band dispersion was computed in the form of *k*-resolved surface PDOS(k, E) maps under a semiinfinite (open boundary) geometry after matching the Hamiltonian of the relaxed slab to that of bulk Ag via Green's functions techniques as explained elsewhere (71). The resolution of the maps was set to 10 meV in energy and 0.006 Å^{-1} in *k* space. For the STM simulations, we modeled the tip apex as a 10-atom silver pyramid, stacked below a semiinfinite Ag(111) surface, and attached to the apex end atom a CO molecule. The elastic current across the STM interface was obtained by following our first-order nonequilibrium Green's function (NEGF) approach (71), assuming a wide band limit for the tip's electronic structure. In all cases the bias was swept between -2 and $+2$ eV, but no significant changes in the aspect of the images were found, in accordance with the experiments.

Finally, the AFM simulations were carried out with Hapala's Probe Particle Model (PPM) code (14) under the Lennard-Jones framework and assuming a CO tip. Default parameters for the probe particle's effective charge (0.0 e), the bending stiffness (0.5 N·m^{-1}), and the particle–tip bond-length stiffness (20 N·m^{-1}) were used throughout. Given the agreement reached with the experimental images, no further refinement of these values was attempted.

Data Availability. The raw data of Figs. 1 *C–F*; 2 *C–F*; 3 *C*, *E*, and *F*; 4 *C*, *E*, and *F*; and 5*C* have been deposited in Zenodo (74). These data include the raw $\Delta f(Z)$ spectra of Figs. 1*F*, 2*F*, 3*F*, 4*F*, and 5*C* as well as the extracted $F(Z)$ curves of *SI Appendix*, Fig. S4 and raw DFT structures displayed in Figs. 1*C*, 2*C*, 3*C*, and 4*C* that were used to generate the AFM simulations of Figs. 1*E*, 2*E*, 3*E*, and 4*E* and band structures of Fig. 6. The experimental STM/AFM images shown throughout this paper and *SI Appendix* are raw data.

ACKNOWLEDGMENTS. E.M., R.P., M.K., C.D., and P.D. thank the Swiss National Science Foundation and the Swiss Nanoscience Institute. E.M., M.K., and R.P. acknowledge funding from the European Research Council under the European Union's Horizon 2020 research and innovation program (Ultrasensitive mechanical dissipation in classical, quantum and non-equilibrium nanocontacts [ULTRADISS] Grant 834402). J.I.C. acknowledges support from the Spanish Ministry of Economy and Competitiveness under Contracts MAT2015-66888-C3-1R and RTI2018-097895-B-C41. We gratefully thank Guy Le Lay for fruitful discussion.

1. A. K. Geim, K. S. Novoselov, The rise of graphene. *Nat. Mater.* **6**, 183–191 (2007).
2. P. Vogt *et al.*, Silicene: Compelling experimental evidence for graphene like two-dimensional silicon. *Phys. Rev. Lett.* **108**, 155501 (2012).
3. M. E. Dávila, L. Xian, S. Cahangirov, A. Rubio, G. L. Lay, Germanene: A novel two-dimensional germanium allotrope akin to graphene and silicene. *New J. Phys.* **16**, 095002 (2014).
4. F. F. Zhu *et al.*, Epitaxial growth of two-dimensional stanene. *Nat. Mater.* **14**, 1020–1025 (2015).
5. A. Molle *et al.*, Buckled two-dimensional Xene sheets. *Nat. Mater.* **16**, 163–169 (2017).
6. C. C. Liu, W. Feng, Y. Yao, Quantum spin Hall effect in silicene and two-dimensional germanium. *Phys. Rev. Lett.* **107**, 076802 (2011).
7. F. J. Giessibl, The qplus sensor, a powerful core for the atomic force microscope. *Rev. Sci. Instrum.* **90**, 011101 (2019).
8. L. Gross, F. Mohn, N. Moll, P. Liljeroth, G. Meyer, The chemical structure of a molecule resolved by atomic force microscopy. *Science* **325**, 1110–1114 (2009).
9. B. J. Albers *et al.*, Three-dimensional imaging of short-range chemical forces with picometre resolution. *Nat. Nanotechnol.* **4**, 307–310 (2009).
10. M. P. Boneschanscher, S. K. Hämäläinen, P. Liljeroth, I. Swart, Sample corrugation affects the apparent bond lengths in atomic force microscopy. *ACS Nano* **8**, 3006–3014 (2014).
11. P. Ruffieux *et al.*, On-surface synthesis of graphene nanoribbons with zigzag edge topology. *Nature* **531**, 489–492 (2016).
12. S. Kawai *et al.*, Multiple heteroatom substitution to graphene nanoribbon. *Sci. Adv.* **4**, eaar7181 (2018).
13. X. Liu *et al.*, Geometric imaging of borophene polymorphs with functionalized probes. *Nat. Commun.* **10**, 1642 (2019).
14. P. Hapala *et al.*, Mechanism of high-resolution STM/AFM imaging with functionalized tips. *Phys. Rev. B* **90**, 085421 (2014).
15. B. Schuler *et al.*, Adsorption geometry determination of single molecules by atomic force microscopy. *Phys. Rev. Lett.* **111**, 106103 (2013).
16. K. Iwata *et al.*, Chemical structure imaging of a single molecule by atomic force microscopy at room temperature. *Nat. Commun.* **6**, 7766 (2015).
17. S. Kawai *et al.*, Organometallic bonding in an Ullmann-type on-surface chemical reaction studied by high-resolution atomic force microscopy. *Small* **12**, 5303–5311 (2016).
18. A. Sweetman *et al.*, Simultaneous noncontact AFM and STM of Ag/Si(111)-($\sqrt{3} \times \sqrt{3}$)$R30^\circ$. *Phys. Rev. B* **87**, 075310 (2013).
19. Y. Sugimoto *et al.*, Chemical identification of individual surface atoms by atomic force microscopy. *Nature* **446**, 64–67 (2007).
20. M. Ellner, P. Pou, R. Pérez, Molecular identification, bond order discrimination, and apparent intermolecular features in atomic force microscopy studied with a charge density based method. *ACS Nano* **13**, 786–795 (2019).
21. F. Liu, C. C. Liu, K. Wu, F. Yang, Y. Yao, $d + id'$ chiral superconductivity in bilayer silicene. *Phys. Rev. Lett.* **111**, 066804 (2013).
22. C. Xu *et al.*, Giant magnetoresistance in silicene nanoribbons. *Nanoscale* **4**, 3111–3117 (2012).
23. M. Ezawa, A topological insulator and helical zero mode in silicene under an inhomogeneous electric field. *New J. Phys.* **14**, 033003 (2012).
24. A. M. Tokmachev *et al.*, Emerging two-dimensional ferromagnetism in silicene materials. *Nat. Commun.* **9**, 1672 (2018).
25. L. Tao *et al.*, Silicene field-effect transistors operating at room temperature. *Nat. Nanotechnol.* **10**, 227–231 (2015).
26. L. Meng *et al.*, Buckled silicene formation on Ir(111). *Nano Lett.* **13**, 685–690 (2013).
27. A. Fleurence *et al.*, Experimental evidence for epitaxial silicene on diboride thin films. *Phys. Rev. Lett.* **108**, 245501 (2012).
28. X. Li *et al.*, Intrinsic electrical transport properties of monolayer silicene and MoS_2 from first principles. *Phys. Rev. B* **87**, 115418 (2013).
29. L. Huang *et al.*, Sequence of silicon monolayer structures grown on a Ru surface: From a herringbone structure to silicene. *Nano Lett.* **17**, 1161–1166 (2017).
30. B. Feng *et al.*, Evidence of silicene in honeycomb structures of silicon on Ag(111). *Nano Lett.* **12**, 3507–3511 (2012).
31. L. Chen *et al.*, Evidence for Dirac fermions in a honeycomb lattice based on silicon. *Phys. Rev. Lett.* **109**, 056804 (2012).
32. C. L. Lin *et al.*, Structure of silicene grown on Ag(111). *Appl. Phys. Exp.* **5**, 045802 (2012).
33. H. Jamgotchian *et al.*, Growth of silicene layers on Ag(111): Unexpected effect of the substrate temperature. *J. Phys. Condens. Matter* **24**, 172001 (2012).
34. R. Arafune *et al.*, Structural transition of silicene on Ag(111). *Surf. Sci.* **608**, 297–300 (2013).
35. Z. Majzik *et al.*, Combined AFM and STM measurements of a silicene sheet grown on the Ag(111) surface. *J. Phys. Condens. Matter* **25**, 225301 (2013).
36. A. Resta *et al.*, Atomic structures of silicene layers grown on Ag(111): Scanning tunneling microscopy and noncontact atomic force microscopy observations. *Sci. Rep.* **3**, 2399 (2013).
37. J. Onoda, K. Yabuoshi, H. Miyazaki, Y. Sugimoto, High-resolution imaging of silicene on an Ag(111) surface by atomic force microscopy. *Phys. Rev. B* **96**, 241302 (2017).
38. L. Feng *et al.*, Structural identification of silicene on the Ag(111) surface by atomic force microscopy. *Phys. Rev. B* **98**, 195311 (2018).
39. D. Tsoutsou, E. Xenogiannopoulou, E. Golias, P. Tsipas, A. Dimoulas, Evidence for hybrid surface metallic band in (4×4) silicene on Ag(111). *Appl. Phys. Lett.* **103**, 231604 (2013).
40. Y. Feng *et al.*, Direct evidence of interaction-induced Dirac cones in a monolayer silicene/Ag(111) system. *Proc. Natl. Acad. Sci. U.S.A.* **113**, 14656–14661 (2016).
41. P. M. Sheverdyaeva *et al.*, Electronic states of silicene allotropes on Ag(111). *ACS Nano.* **11**, 975–982 (2017).
42. C. L. Lin *et al.*, Substrate-induced symmetry breaking in silicene. *Phys. Rev. Lett.* **110**, 076801 (2013).
43. Y. Fukaya *et al.*, Structure of silicene on a Ag(111) surface studied by reflection high–energy positron diffraction. *Phys. Rev. B* **88**, 205413 (2013).
44. K. Kawahara *et al.*, Determination of atomic positions in silicene on Ag(111) by low-energy electron diffraction. *Surf. Sci.* **623**, 25–28 (2014).
45. H. Enriquez, S. Vizzini, A. Kara, B. Lalmi, H. Oughaddou, Silicene structures on silver surfaces. *J. Phys. Condens. Matter* **24**, 314211 (2012).
46. Z. X. Guo, S. Furuya, J. I. Iwata, A. Oshiyama, Absence of Dirac electrons in silicene on Ag(111) surfaces. *J. Phys. Soc. Japan* **82**, 063714 (2013).
47. E. Scalise *et al.*, Vibrational properties of silicene and germanene. *Nano Res.* **6**, 19–28 (2013).
48. H. Jamgotchian *et al.*, A comprehensive analysis of the ($\sqrt{13} \times \sqrt{13}$)R13.9° type II structure of silicene on Ag(111). *J. Phys. Condens. Matter* **28**, 195002 (2016).
49. M. R. Tchalala *et al.*, Atomic and electronic structures of the ($\sqrt{13} \times \sqrt{13}$)R13.9° of silicene sheet on Ag(111). *Appl. Surf. Sci.* **303**, 61–66 (2014).
50. P. Vogt *et al.*, Synthesis and electrical conductivity of multilayer silicene. *Appl. Phys. Lett.* **104**, 021602 (2014).
51. J. Sone, T. Yamagami, Y. Aoki, K. Nakatsuji, H. Hirayama, Epitaxial growth of silicene on ultra-thin Ag(111) films. *New J. Phys.* **16**, 095004 (2014).
52. G. Prévot, R. Bernard, H. Cruguel, Y. Borensztein, Monitoring Si growth on Ag(111) with scanning tunneling microscopy reveals that silicene structure involves silver atoms. *Appl. Phys. Lett.* **405**, 213106 (2014).

53. Y. Borensztein, A. Curcella, S. Royer, G. Prévot, Silicene multilayers on Ag(111) display a cubic diamondlike structure and a $\sqrt{3} \times \sqrt{3}$ reconstruction induced by surfactant Ag atoms. *Phys. Rev. B* **92**, 155407 (2015).
54. R. Bernard, Y. Borensztein, H. Cruguel, M. Lazzeri, G. Prévot, Growth mechanism of silicene on Ag(111) determined by scanning tunneling microscopy measurements and ab initio calculations. *Phys. Rev. B* **92**, 045415 (2015).
55. R. Bernard *et al.*, Growth of Si ultrathin films on silver surfaces: Evidence of an Ag(110) reconstruction induced by Si. *Phys. Rev. B* **88**, 121411 (2013).
56. J. I. Cerdá *et al.*, Unveiling the pentagonal nature of perfectly aligned single- and double-strand Si nanoribbons on Ag(110). *Nat. Commun.* **7**, 13076 (2016).
57. A. Curcella *et al.*, Determining the atomic structure of the (4×4) silicene layer on Ag(111) by combined grazing-incidence X-ray diffraction measurements and first-principles calculations. *Phys. Rev. B* **94**, 165438 (2016).
58. H. Jamgotchian *et al.*, A comprehensive study of the $(2\sqrt{3} \times 2\sqrt{3})R30^\circ$ structure of silicene on Ag(111). *J. Phys. Condens. Matter* **27**, 395002 (2015).
59. Z. L. Liu *et al.*, Various atomic structures of monolayer silicene fabricated on Ag(111). *New J. Phys.* **16**, 075006 (2014).
60. P. Pflugradt, L. Matthes, F. Bechstedt, Silicene-derived phases on Ag(111) substrate versus coverage: Ab initio studies. *Phys. Rev. B* **89**, 035403 (2014).
61. A. Curcella *et al.*, Structure and stability of silicene on Ag(111) reconstructions from grazing incidence X-ray diffraction and density functional theory. *Phys. Rev. B* **99**, 205411 (2019).
62. J. Gao, J. Zhao, Initial geometries, interaction mechanism and high stability of silicene on Ag(111) surface. *Sci. Rep.* **2**, 861 (2012).
63. S. Li *et al.*, Defects in silicene: Vacancy clusters, extended line defects, and di-adatoms. *Sci. Rep.* **5**, 7881 (2015).
64. D. Ghosh, P. Parida, S. K. Pati, Stable line defects in silicene. *Phys. Rev. B* **92**, 195136 (2015).
65. L. Bartels *et al.*, Dynamics of electron-induced manipulation of individual CO molecules on Cu(111). *Phys. Rev. Lett.* **80**, 2004–2007 (1998).
66. Z. Sun, M. P. Boneschanscher, I. Swart, D. Vanmaekelbergh, P. Liljeroth, Quantitative atomic force microscopy with carbon monoxide terminated tips. *Phys. Rev. Lett.* **106**, 046104 (2011).
67. L. Gross *et al.*, Bond-order discrimination by atomic force microscopy. *Science* **337**, 1326–1329 (2012).
68. J. E. Sader, S. P. Jarvis, Accurate formulas for interaction forces and energy in frequency modulation force spectroscopy. *Appl. Phys. Lett.* **84**, 1801–1803 (2004).
69. B. W. H. van Beest, G. J. Kramer, R. A. van Santen, Force fields for silicas and aluminophosphates based on ab initio calculations. *Phys. Rev. Lett.* **64**, 1955 (1990).
70. R. A. Buckingham, The classical equation of state of gaseous helium, neon and argon. *Proc. R. Soc. Lond. Ser. A* **168**, 264–283 (1938).
71. E. T. R. Rossen, C. F. J. Flipse, J. Cerdá, Lowest order in inelastic tunneling approximation: Efficient scheme for simulation of inelastic electron tunneling data. *Phys. Rev. B* **87**, 235412 (2013).
72. J. M. Soler *et al.*, The SIESTA method for ab initio order-n materials simulation. *J. Phys. Condens. Matter* **14**, 2745–2779 (2002).
73. J. P. Perdew, K. Burke, M. Ernzerhof, Generalized gradient approximation made simple. *Phys. Rev. Lett.* **77**, 3865–3868 (1996).
74. R. Pawlak *et al.*, Quantitative determination of atomic buckling of silicene by atomic force microscopy. Zenodo. https://zenodo.org/record/3501355. Deposited 18 October 2019.